materials

MDPI

Article

Electrochemically Inert Li_2MnO_3: The Key to Improving the Cycling Stability of Li-Rich Manganese Oxide Used in Lithium-Ion Batteries

Lian-Bang Wang, He-Shan Hu, Wei Lin, Qing-Hong Xu, Jia-Dong Gong, Wen-Kui Chai and Chao-Qi Shen *

State Key Laboratory Breeding Base of Green Chemistry-Synthesis Technology, College of Chemical Engineering, Zhejiang University of Technology, Hangzhou 310014, China; wanglb99@zjut.edu.cn (L.-B.W.); zjuthuheshan@163.com (H.-S.H.); 2112001474@zjut.edu.cn (W.L.); 2111901309@zjut.edu.cn (Q.-H.X.); 2111901065@zjut.edu.cn (J.-D.G.); kikiihac@gmail.com (W.-K.C.)
* Correspondence: shenchaoqi@zjut.edu.cn

Abstract: Lithium-rich manganese oxide is a promising candidate for the next-generation cathode material of lithium-ion batteries because of its low cost and high specific capacity. Herein, a series of $xLi_2MnO_3 \cdot (1 - x)LiMnO_2$ nanocomposites were designed via an ingenious one-step dynamic hydrothermal route. A high concentration of alkaline solution, intense hydrothermal conditions, and stirring were used to obtain nanoparticles with a large surface area and uniform dispersity. The experimental results demonstrate that $0.072Li_2MnO_3 \cdot 0.928LiMnO_2$ nanoparticles exhibit a desirable electrochemical performance and deliver a high capacity of 196.4 mAh g^{-1} at 0.1 C. This capacity was maintained at 190.5 mAh g^{-1} with a retention rate of 97.0% by the 50th cycle, which demonstrates the excellent cycling stability. Furthermore, XRD characterization of the cycled electrode indicates that the Li_2MnO_3 phase of the composite is inert, even under a high potential (4.8 V), which is in contrast with most previous reports of lithium-rich materials. The inertness of Li_2MnO_3 is attributed to its high crystallinity and few structural defects, which make it difficult to activate. Hence, the final products demonstrate a favorable electrochemical performance with appropriate proportions of two phases in the composite, as high contents of inert Li_2MnO_3 lower the capacity, while a sufficient structural stability cannot be achieved with low contents. The findings indicate that controlling the composition through a dynamic hydrothermal route is an effective strategy for developing a Mn-based cathode material for lithium-ion batteries.

Keywords: lithium-rich manganese oxide; nanocomposite; dynamic hydrothermal; inert Li_2MnO_3; cycling stability

Citation: Wang, L.-B.; Hu, H.-S.; Lin, W.; Xu, Q.-H.; Gong, J.-D.; Chai, W.-K.; Shen, C.-Q. Electrochemically Inert Li_2MnO_3: The Key to Improving the Cycling Stability of Li-Rich Manganese Oxide Used in Lithium-Ion Batteries. *Materials* **2021**, *14*, 4751. https://doi.org/10.3390/ma14164751

Academic Editors: Federico Bella and Changshin Jo

Received: 7 July 2021
Accepted: 21 August 2021
Published: 23 August 2021

1. Introduction

Since rechargeable lithium-ion batteries were first applied to electronic products in the 1990s, their development has been continual [1]. After three decades, Li-ion batteries have evolved and become an essential component of well-established energy storage strategies, with excellent efficiency in terms of energy and power densities, life span, and design flexibility [2,3]. Meanwhile, the storage demand from clean energy technologies requires Li-ion batteries, given their merits of low cost, high safety, and environmental compatibility [4]. Compared with new generation anode materials, such as silicon–carbon composites with a specific capacity of 700–2000 mAh g^{-1}, improvement in the capacity of cathode materials is somewhat lagging [5,6]. As the bottleneck of capacity and energy density, cathode materials are believed to be the main factor when further optimizing the electrochemical performance and addressing other issues of Li-ion batteries [5,7].

Currently, the most widely used cathode materials are ternary NMC and $LiFePO_4$, while Li-rich manganese-based materials have attracted considerable attention due to their low cost and high specific capacity. Generally, this type of cathode material, noted

as $xLi_2MnO_3 \cdot (1 - x)LiTMO_2$ (transition metal (TM) = Ni, Co, and Mn, etc.), exhibits a superior specific capacity (>250 mAh g^{-1}) and high operation voltage to realize an excellent energy density; thus, $xLi_2MnO_3 \cdot (1 - x)LiTMO_2$ is assumed to be a promising cathode material for the next generation of lithium-ion batteries [8]. However, the large price fluctuation of cobalt and nickel in recent years, as well as their negative impact on the environment, have driven researchers to design Li-rich manganese oxide without Ni and Co, using $xLi_2MnO_3 \cdot (1 - x)LiMnO_2$ as a substitute [9,10]. The preparation routes of $xLi_2MnO_3 \cdot (1 - x)LiMnO_2$ include solid-state calcination [11], sol–gel synthesis [12], pyrolysis reduction [13], and hydrothermal/solvothermal reaction [14]. The specific capacity of $xLi_2MnO_3 \cdot (1 - x)LiMnO_2$ has been significantly improved in comparison with common lithium manganese oxides ($LiMn_2O_4$, $LiMnO_2$), but its capacity degradation during cycling is relatively severe [15].

The structure of the xLi_2MnO_3 $(1 - x)LiMnO_2$ composite is believed to be a mixture of the Li_2MnO_3 and $LiMnO_2$ crystal domains [16,17], while the hypothesis of a solid-state solution has also been presented in some studies [18,19]. In the composite, the crystal structure of Li_2MnO_3 is combined with monoclinic C2/m, but $LiMnO_2$ can display diverse structures, such as monoclinic or orthorhombic structures, when using different synthetic methods. In most publications, Li_2MnO_3 was activated in the initial cycles and provided an extra capacity, similarly to $xLi_2MnO_3 \cdot (1 - x)LiTMO_2$ mentioned above. During the activation process, the conjoint removal of Li^+ and O forms an active "MnO_2-like" phase, and anionic and cationic vacancies are generated simultaneously to cause lattice densification [20,21]. Irreversible O_2 extraction ($Li_2MnO_3 \rightarrow Li_xMnO_2 + (2 - x)Li^+ + 1/2O_2 + (2 - x)e^-$), occupation of the Li^+ site by the transition metal, and phase transformation to spinel or rock salt induce a decline in capacity [22–24]. While recent research has demonstrated that Li_2MnO_3 is activated to generate oxygen anion O^{n-} ($n < 2$), redox of the oxygen anion during cycling could contribute considerably to increasing its capacity [25]. In order to improve the stability of the material and to mitigate the reduction in capacity due to structure evolution, elemental doping and surface modification with oxides are widely applied [26]. However, applying additional optimization treatment procedures generally goes against attempts to develop cost-effective and time-saving methods for the production of cathode materials [27].

In this work, a $xLi_2MnO_3 \cdot (1 - x)LiMnO_2$ composite was prepared via a one-step dynamic hydrothermal synthetic route; interestingly, the contained Li_2MnO_3 was not activated even when cycled under 2–4.8V for 15 cycles. The x-values of 0.045, 0.072, and 0.114 in $xLi_2MnO_3 \cdot (1 - x)LiMnO_2$ were characterized by ICP–OES, and the sample containing 0.072 Li_2MnO_3 manifested the best electrochemical performance. The inertness of Li_2MnO_3 is ascribed to its high crystallinity with few defects, as its presence effectively improved the electrochemical cycling capability of $xLi_2MnO_3 \cdot (1 - x)LiMnO_2$ due to its structural stability. The mechanism still requires further investigation, however, this research provides a novel method to synthesize $xLi_2MnO_3 \cdot (1 - x)LiMnO_2$ cathode material with a low cost and a stable cycling capability for application in lithium-ion batteries.

2. Materials and Methods

The samples were prepared via a one-step dynamic hydrothermal method. MnO_2, $Mn(CH_3COO)_2 \cdot 4H_2O$, $LiOH \cdot H_2O$, and NaOH were purchased from Aladdin (Shanghai, China). The preparation procedure is described briefly, as follows: 0.04 mol MnO_2, 0.04 mol $Mn(CH_3COO)_2 \cdot 4H_2O$, 0.24 mol $LiOH \cdot H_2O$, 0.36 mol NaOH, and 200 mL deionized water were mixed in a 1000 mL dynamic autoclave with a stirrer (stirring rate of 150 rpm). The hydrothermal treatment was carried out at 200 °C for 5 h, with the temperature being increased at a rate of 2 °C min^{-1}. Following the reaction, the autoclave was left to cool down to room temperature under ambient conditions. The sample was collected by centrifugation and was washed with deionized water several times, then dried at 80 °C overnight. The final product was marked as LMO-1. LMO-2 and LMO-3 were obtained with the same reagent concentrations, while the volume of solutions were set to 400 and 600 mL of H_2O,

respectively. Furthermore, with the purpose of controlling the atmosphere in the reaction system, the gas in the autoclave was sufficiently purged by compressed air before the hydrothermal process. For use in comparisons, pure o-$LiMnO_2$ (marked as LMO-P) was synthesized using ethylene diamine tetraacetic acid disodium salt (EDTA-2Na) according to a previous report [28].

The crystal structures were evaluated by powder X-ray diffraction (XRD; X'Pert Pro, PANalytical, Almelo, The Netherlands) with Cu Kα radiation over the range of 2θ = 10–80°. The morphologies of the samples were investigated using scanning electron microscopy (SEM; Nova NanoSEM 450, FEI company, Hillsboro, OR, USA) and transmission electron microscopy (TEM; Tecnai G2F30 S-Twin operated at 300 kV, FEI company, Hillsboro, OR, USA). The size distribution of the samples was analyzed using a particle dimension laser analyzer in dry mode (LS230, Beckman Coulter, Brea, CA, USA). The chemical valence state of the Mn element was confirmed by XPS (Thermo Scientific K-Alpha, Thermo Fisher Scientific, Waltham, MA, USA). The elemental ratio of the samples was analyzed by inductively coupled plasma optical emission spectrometry (ICP–OES, Agilent 720ES, Agilent Technologies, Santa Clara, CA, USA).

The contents of Mn^{3+} and Mn^{4+} from the various samples were obtained via chemical titration according to previous works [29,30]. The final results were the mean values of the triplicate experiments. Chrome blue black R, sulfuric acid, sodium oxalate benchmark solution, EDTA, ammonia–ammonium chloride buffer solution, and ammonium sulfate solution were used in the titration.

The electrochemical performance of the samples was measured using the 2032-type coin cell. A slurry composed of 10 wt.% binder (polyvinylidene fluoride (PVDF)), 10 wt.% conductive additive (Super P Li carbon black), and 80 wt.% active material in N-methyl-2-pyrrolidone (NMP) was cast onto aluminum foil. The electrodes were approximately 100 μm thick and the loading mass of the active material was approximately 1.5 mg cm^{-2}. The half-cells were assembled in an argon-filled glovebox employing pure lithium foil as anodes and Celgard 2400 membranes as separators. The electrolyte was composed of a solution of $LiPF_6$ (1 M) in ethylene carbonate, ethyl methyl carbonate, and dimethyl carbonate (1:1:1 by volume). The coin cells were galvanostatically cycled on a CT2001A (LAND Electronic Co., Wuhan, China) multi-channel battery test system at room temperature. A cyclic voltammetry (CV) test was conducted on an Ivium electrochemical workstation (Ivium-n-Stat, IVIUM Technologies, Eindhoven, Netherlands) at a scan rate of 0.1 mV s^{-1} between 2.0 and 4.8 V. The electrochemical impedance spectra (EIS) were collected by the Ivium workstation (Ivium-n-Stat, IVIUM Technologies, Eindhoven, Netherlands) within the frequency range of 0.01 Hz–100 kHz with an amplitude of 10 mV.

3. Results and Discussion

The high crystallinity and phase composition of the hydrothermally synthesized $xLi_2MnO_3 \cdot (1 - x)LiMnO_2$ samples were distinctly confirmed by XRD measurement (Figure 1a). The diffraction peaks of $LiMnO_2$ can be indexed to the α-$NaFeO_2$-type layered structure with a space group of R3m. Meanwhile, the intensity of the peaks at 18.7° and 44.7° can be ascribed to Li_2MnO_3 with the C/2m space group, declining gradually as the oxygen in the autoclave decreased, which was more obvious in the enlarged interval between 42° and 48° (Figure 1b). This trend can be attributed to residual oxygen in the reaction system inevitably producing Li_2MnO_3, and the chemical reaction can be formulated as follows:

$$Mn(II) + MnO_2 + 4Li^+ + 6OH^- + 1/2O_2 \rightarrow 2Li_2MnO_3 + 3H_2O$$

The ICP–OES results in Table 1 present the molar ratio of Li and Mn with the calculation of the Mn valance. The x-values in LMO-1, LMO-2, and LMO-3 are 0.114, 0.072, and 0.045, respectively. Meanwhile, in LMO-P, the content of Li_2MnO_3 is only 0.9%, which can be regarded as pure $LiMnO_2$. The ratio of the two phases from the different samples is displayed in Figure 1c. In addition, the Mn valence state (Mn^{3+} and Mn^{4+}) in each sample was

tested using the chemical titration method, and the results are shown in Table 2. According to the chemical titration results, the composition of the $xLi_2MnO_3 \cdot (1-x)LiMnO_2$ samples is in accordance with the ICP–OES characterization.

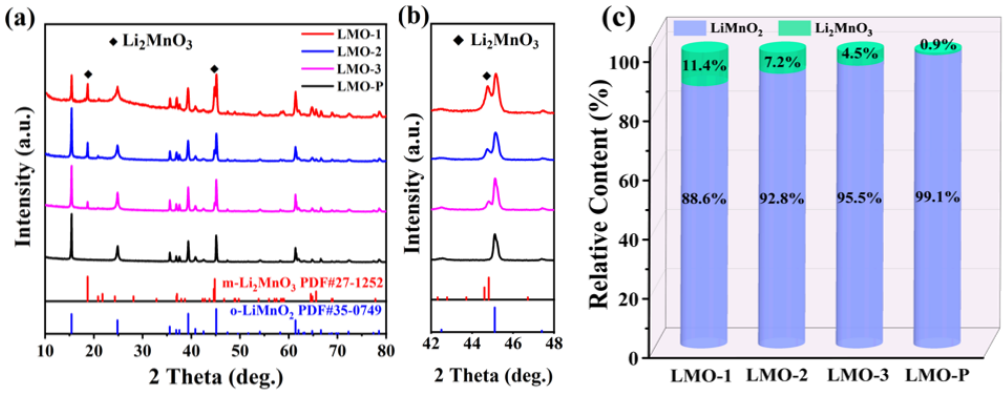

Figure 1. The XRD patterns (**a**,**b**) and ratio of the two phases (**c**) of the four synthesized samples.

Table 1. The experimental results of the Li/Mn atom ratio, e Mn average valance, and corresponding calculated x-values.

Sample	Li/Mn $_{exp}$	Li/Mn $_{theoretical}$	Mn Valance $_{exp}$	x Values in $xLi_2MnO_3 \cdot (1-x)LiMnO_2$
o-$LiMnO_2$	1	1	3	0
Li_2MnO_3	2	2	4	1
LMO-1	1.114	\	3.114	0.114
LMO-2	1.072	\	3.072	0.072
LMO-3	1.045	\	3.045	0.045
LMO-P	1.009	\	3.009	0.009

Table 2. Different manganese valences and their respective content obtained using the chemical titration method, and the composition of $xLi_2MnO_3 \cdot (1-x)LiMnO_2$.

Sample	Mn^{3+}	Mn^{4+}	x-Values in $xLi_2MnO_3 \cdot (1-x)LiMnO_2$
LMO-1	88.8%	11.2%	0.112
LMO-2	92.9%	7.1%	0.071
LMO-3	95.3%	4.7%	0.047
LMO-P	99.3%	0.7%	0.007

Figure 2 presents the XPS spectra of four samples, where the chemical state of Mn 2p can be clarified as the combination of Mn^{4+} ($2p_{3/2}$ 643.4 eV) and Mn^{3+} ($2p_{3/2}$ 641.7 eV) [31,32]. The Mn^{4+} content decreased with the decline of oxygen in the reaction system, as reflected by the less Li_2MnO_3 in the final product. The area of fitted XPS curves indicates that Mn^{3+} is the majority species, while the Mn in LMO-P sample can be regarded as Mn^{3+} entirely, a conclusion that is consistent with the XRD and ICP results.

The SEM images of four products are presented in Figure 3a–d, all of which show similar morphologies with a particle size ranging from 30 to 150 nm. The size distribution was further examined using a laser particle size analyzer (Figure 3f–i), in which the mean sizes of 81.4, 82.3, 80.9, and 82.1 nm were determined for LMO-1, LMO-2, LMO-3, and LMO-P, respectively. The particle size of the synthesized products is smaller than reported before [11,12]. The use of an alkaline solution with stirring established an appropriate reaction environment for generating nanoparticles with a large surface area and to prevent agglomeration. Hence, the contact area between the active material and electrolyte was enlarged, which produced a shorter diffusion path for Li^+ to minimize polarization during charging–discharging [33].

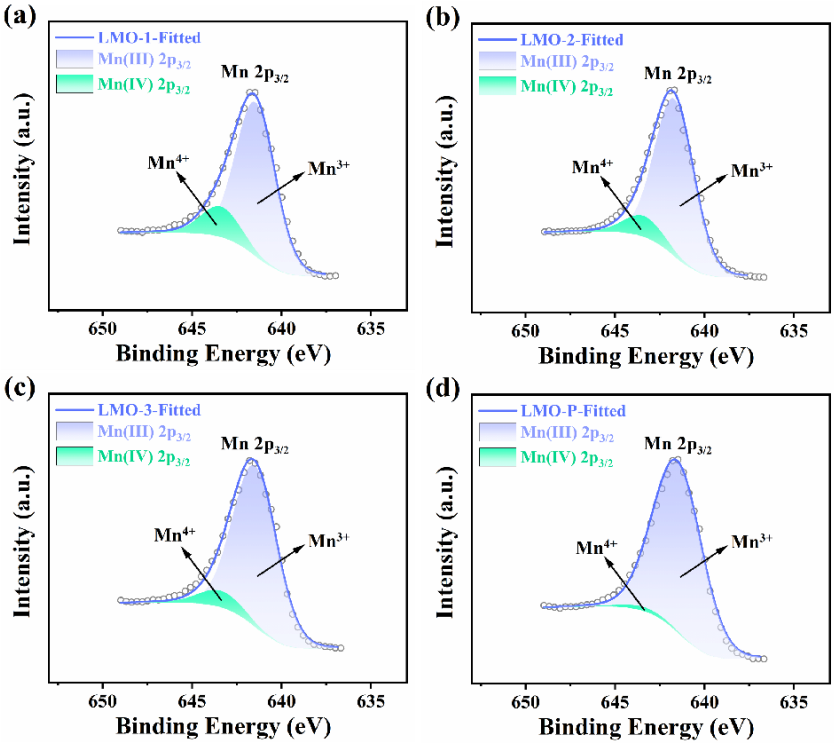

Figure 2. The XPS spectra of the various samples (**a**–**d**).

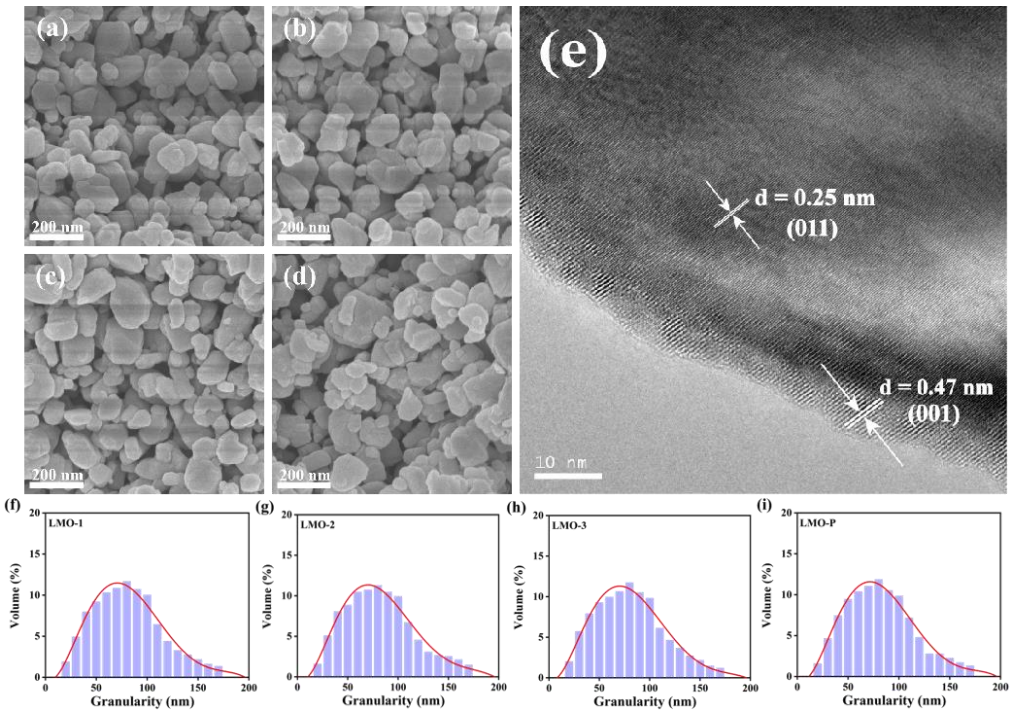

Figure 3. The SEM images of the various samples (**a**–**d**), TEM image of LMO-2 (**e**), and particle size distribution of the samples (**f**–**i**).

The HRTEM image of LMO-2 in Figure 3e exhibits lattice fringes with an interplanar space of 0.25 nm, assigned to the (011) crystal plane of orthorhombic $LiMnO_2$, and lattice fringes with 0.47 nm of the (001) crystal plane from Li_2MnO_3, which confirm the good crystallinity of the product and the co-existence of the two phases. The lattice fringe spacings of $LiMnO_2$ (011) and Li_2MnO_3 (001) were also calculated based on the XRD pattern of LMO-2. According to the Bragg equation, $2d\sin\theta = n\lambda$ (n = 1), the peak at

2θ = 18.7° with a lattice fringe spacing of 4.74Å corresponds to Li_2MnO_3 (001), while that at 2θ = 35.6° of 2.52Å is $LiMnO_2$ (011), in accordance with HRTEM.

Figure 4 displays the cyclic voltammograms (CVs) of the various samples in the potential interval from 2.0 to 4.8 V at a scan rate of 0.1 mV s^{-1}. The intense oxidation peak at 3.5–4.1 V observed in the first cycle is interpreted as an irreversible de-lithiation from the octahedral sites of $LiMnO_2$ upon charging [31,34]. Generally, the products with Li_2MnO_3 presented another oxidation peak around 4.7 V due to the activation of Li_2MnO_3 with Li^+ extraction and anion oxidation [34,35]. However, this behavior cannot be distinguished in our research, which demonstrates that the Li_2MnO_3 generated via our route is electrochemically inert, even under a high potential. Furthermore, the redox peaks around 3.0 V are ascribed to $Mn^{3+}/Mn^{3.5+}$ in $Li_2Mn_2O_4$ transformed from initial $LiMnO_2$ for all of the samples [36]. In the first charging step, this can be explained by the de-lithiation of Li^+ from octahedral sites and the subsequent migration of Mn^{3+} from the original octahedral sites to neighboring vacant octahedral sites. When Li^+ intercalates into the de-lithiated matrix in the discharge step, it cannot re-insert into the original octahedral sites, but instead forms tetragonal $Li_2Mn_2O_4$ [37,38]. Two peaks characteristic of cubic spinel $LiMn_2O_4$ could be detected at 3.95 and 4.10 V for LMO-2, LMO-3, and LMO-P (Figure 4b–d) [39,40]. While for LMO-1 (Figure 4a), these two peaks are merged, this phenomenon should be ascribed to the higher content of inert Li_2MnO_3 influencing the lithium ion de-intercalation process in spinel $LiMn_2O_4$ [41].

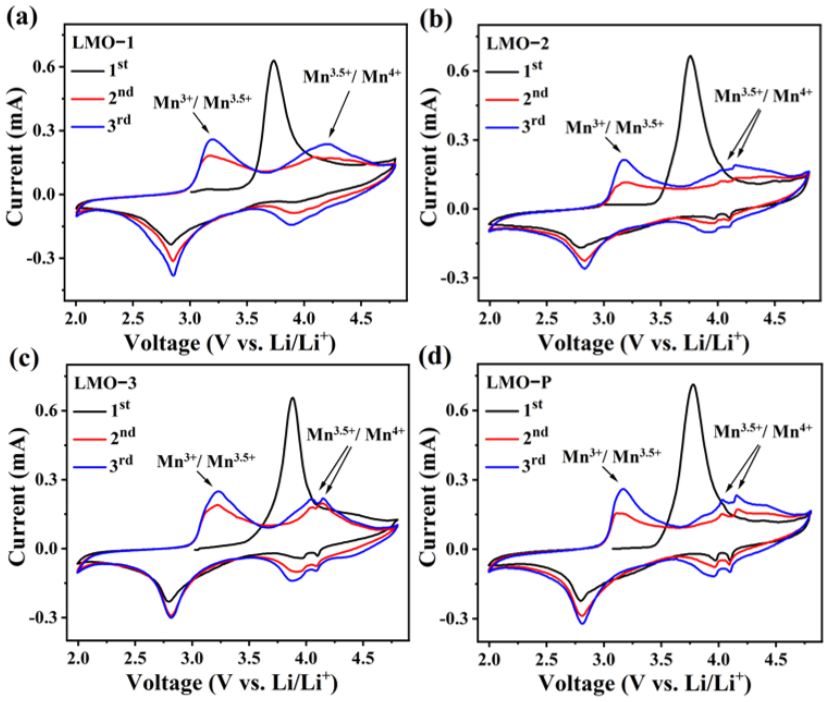

Figure 4. Cyclic voltammograms (CVs) of the various samples in the potential range of 2.0–4.8 V (**a**–**d**).

The charge/discharge profiles of the first cycle are displayed in Figure 5a. The initial charge and discharge plateaus at 3.6 and 3.0 V are characteristic of o-$LiMnO_2$, akin to previous reports and in agreement with the results observed by CV [28]. The discharging capacity and coulombic efficiency of the initial cycle is 90.3 mAh g^{-1} (62.2%), 100.3 mAh g^{-1} (66.4%), 111.2 mAh g^{-1} (70.4%), and 126.4 mAh g^{-1} (72.4%) for LMO-1, LMO-2, LMO-3, and LMO-P, respectively. The capacity of each sample is directly proportional to the content of $LiMnO_2$, and the coulombic efficiency of the initial cycle declined with the increase in the Li_2MnO_3 phase. Such a phenomenon is ascribed to the existence of Li_2MnO_3, hindering the de-intercalation of lithium-ion and impeding the phase transformation from $LiMnO_2$ to $Li_2Mn_2O_4$, thus resulting in a low coulombic efficiency. However, once the $LiMnO_2$ is

entirely transformed to $Li_2Mn_2O_4$, the existence of Li_2MnO_3 was beneficial for preventing structural distortion and improving cycling stability. Furthermore, no obvious peak was present in the related dQ/dV curves in the high potential range of 4.5–4.8 V (Figure 5b). As previously reported, the electrochemical activity of Li_2MnO_3 is induced by structural defects, and with more stacking faults, Li_2MnO_3 is more easily activated to offer extra capacity, and even the activation the voltage plateau was not obvious [42,43]. However, this is inconsistent with our experimental results, where the highest capacity decreased with the increase in Li_2MnO_3 content; thus, the contribution of Li_2MnO_3 activation to increasing capacity could be excluded, and the inertness of Li_2MnO_3 was confirmed.

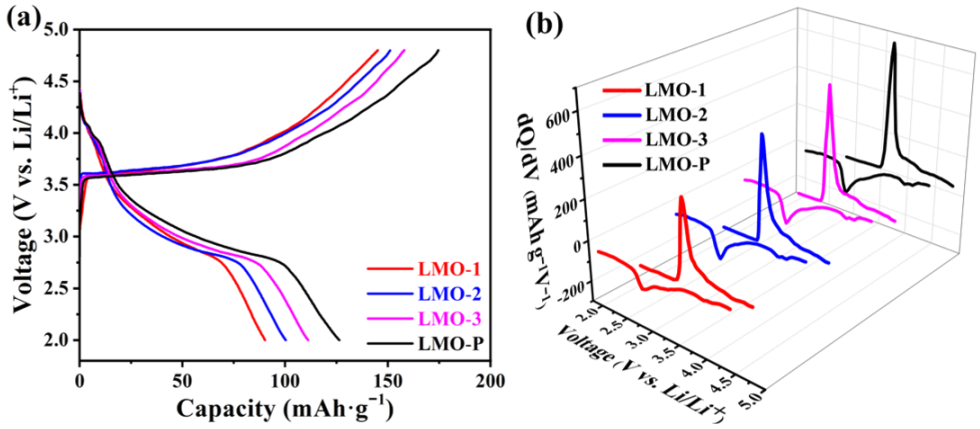

Figure 5. The charge/discharge profiles of the various samples in the first cycle (**a**) and the corresponding dQ/dV curves (**b**).

Plots of the cycling performance of the synthesized materials at 0.1 C (1 C = 300 mA g^{-1}) at ranges of 2.0–4.5 and 2.0–4.8 V are shown in Figure 6a,b. Under both conditions, the capacity gradually increased in the initial cycles, which can be attributed to the increasing content of $Li_2Mn_2O_4$ upon o-$LiMnO_2$ transformation [44]. In comparison, the samples cycled with 2.0–4.8 V presented a higher capacity, which is usually explained by the activation of Li_2MnO_3 at a high potential to offer extra capacity. Nevertheless, the inertness of Li_2MnO_3 in our research implies that more sufficient de-intercalation of Li^+ at a high potential is responsible for the increase in capacity. This could also explain why the highest capacity decreases with an increase in Li_2MnO_3 content.

The speed of the phase transformation from o-$LiMnO_2$ to $Li_2Mn_2O_4$ is related to the content of Li_2MnO_3 in the composite [13]. It is clear that LMO-P reached the highest capacity of 206.1 mAh g^{-1} in six cycles with a potential range of 2.0–4.8 V, while the capacity of the 50th cycle was only 161.5 mAh g^{-1} with a retention rate of 78.4%. In comparison, LMO-1, LMO-2, and LMO-3 achieved higher capacities of 189.4, 196.4, and 197.6 mAh g^{-1} in the 33rd, 19th, and 17th cycles, respectively, and the retention rates of the corresponding samples were 97.3%, 97.0%, and 89.5%, respectively. The cycling performance at a rate of 1 C after activation at 0.1 C for 15 cycles is displayed in Figure 6c. The results show that the capacity retention of LMO-P degraded to 60.3%, while LMO-1, LMO-2, and LMO-3 maintained 95.4%, 89.1%, and 73.3%, respectively. The higher charging–discharging rate demands faster Li^+ de-intercalation and, thus, the structure of a cathode material must be well stabilized, and the existence of Li_2MnO_3 effectively improved this factor. The different cycling capability demonstrates that the existence of inert Li_2MnO_3 improved the structural stability of the material with deep de-lithiation. Meanwhile, the ratio of Li_2MnO_3 in the composite should be optimized to balance the capacity property and the cycling stability, thus achieving the best electrochemical performance; from this point of view, LMO-2 with 7.2% Li_2MnO_3 is the most appropriate choice.

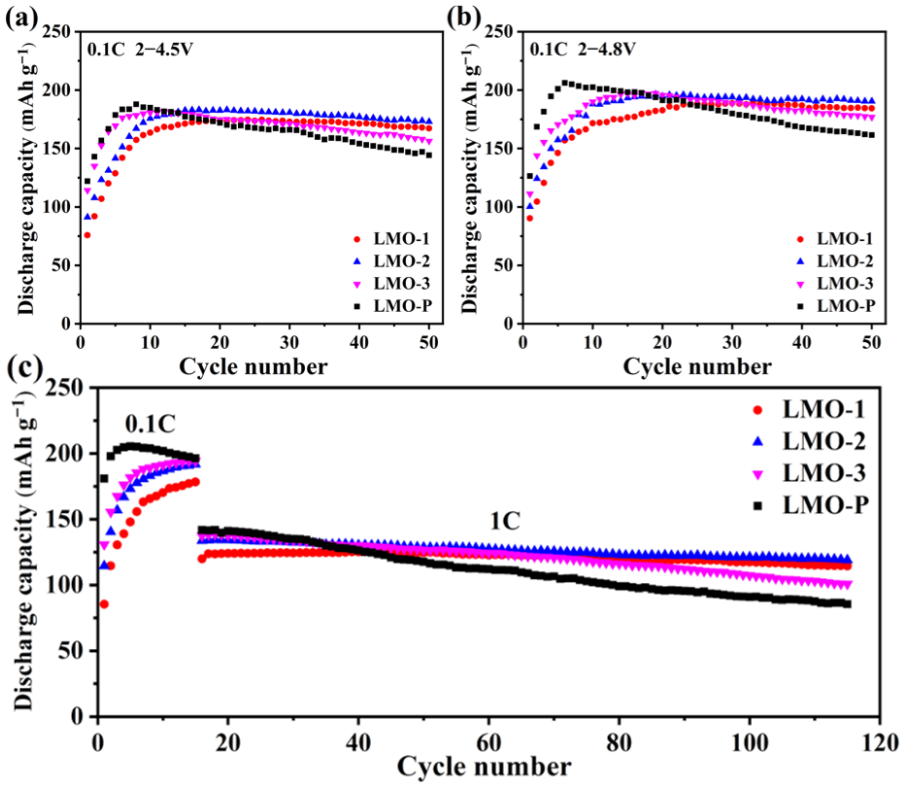

Figure 6. Cycling performance at 0.1 C with the 2.0–4.5 V range (**a**), 0.1 C with the 2.0–4.8 V range (**b**), and 1 C with the 2.0–4.8 V range (**c**).

In fact, the capacity degradation associated with $LiMnO_2$ is due to Mn dissolution and irreversible layer-to-spinel transformation stemming from Jahn–Teller distortion [40,45]. The introduction of a Li_2MnO_3 phase could increase the mean valence of Mn to suppress the disproportionate reaction of Mn^{3+}; more importantly, the layered structure is compatible with $LiMnO_2$ and the stable layered complex structure can effectively delay irreversible transformation to spinel $LiMn_2O_4$ [13,46].

The charging–discharging curves of different materials in the 50th cycle are shown in Figure 7, in which the voltage hysteresis can be detected. As mentioned earlier, the structure of $LiMnO_2$ is transformed and collapses during cycling, and the diffusion path of the lithium-ion then changes to cause voltage hysteresis. In comparison, the existence of Li_2MnO_3 relieves voltage hysteresis under either high or low voltage for the redox reaction of $Mn^{3.5+/4+}$ and $Mn^{3+/3.5+}$, which illustrates that Li_2MnO_3 suppresses further structural distortion of the material.

In order to identify the structural evolution of the composite, ex situ XRD measurements were taken for the discharged LMO-2 cathode disk after 15 cycles, as shown in Figure 8. The o-$LiMnO_2$ phase remarkably vanished, whereas newly formed phases of cubic $LiMn_2O_4$ and tetragonal $Li_2Mn_2O_4$ could be detected. Moreover, the existence of a Li_2MnO_3 phase can be confirmed, which means that Li_2MnO_3 did not participate in the electrochemical reaction. The amount of cubic $LiMn_2O_4$ illustrates that inert Li_2MnO_3 is not capable of thoroughly suppressing phase transformation, while structure distortion and collapse are prevented, resulting in an improved cycling stability.

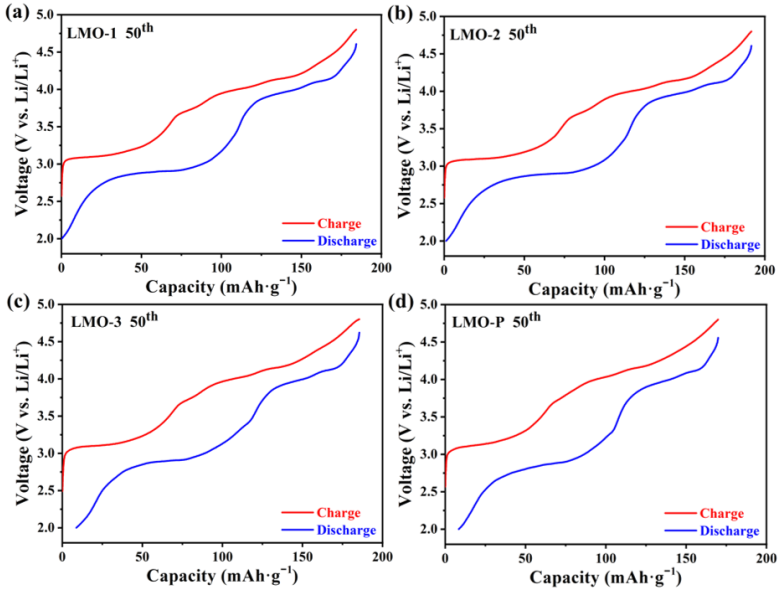

Figure 7. The charging–discharging curves of various samples in the 50th cycle at potential range of 2.0−4.8 V (**a**–**d**).

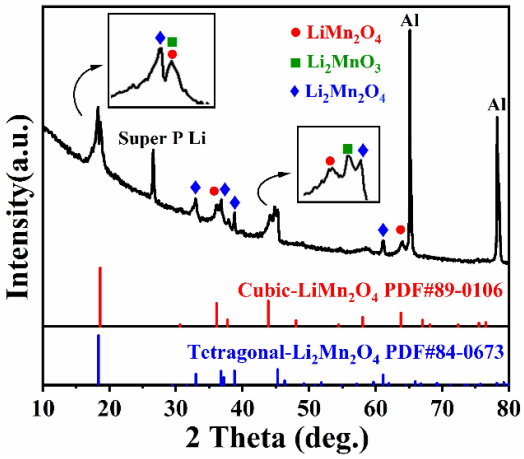

Figure 8. The XRD pattern of the discharged LMO-2 cathode disk after 15 cycles.

The electrochemical impedance spectra (EIS) of the samples before and after cycling are shown in Figure 9. The semicircle of a high frequency is ascribed to the surface film resistance (R_f) formed by the decomposition of the electrolyte, while the semicircle of a high- to medium-frequency represents the charge–transfer resistance (R_{ct}) of the electrochemical process, and the line in the low-frequency range indicates a diffusion-controlled process in the solid electrode [47,48]. The fitted values of the simulated circuit displayed in Table 3 demonstrate a decrease in R_{ct} after cycling, which is attributed to the better electronic and ionic conductivity of the transformed $LiMn_2O_4$ phase with a three-dimensional spinel structure [49]. Furthermore, both before and after cycling, the values of R_{ct} were higher for the sample with more Li_2MnO_3; this phenomenon implies the inferior conductivity of Li_2MnO_3 and that Li_2MnO_3 does not change the state even after being cycled under a high potential. On the contrary, R_s corresponds to the resistance of the cell, which consists of electrolyte resistance and circuit ohmic resistance. It is supposed that after cycling, the battery is aged, and the electrolyte is partially decomposed to generate impurity, thereby obstructing ion transfer to increase the value of R_s, as shown in Table 3 [50]. Meanwhile, the formation of an SEI film on the electrode surface blocking the transfer of Li^+ results in the emergence of R_f compared to the EIS before cycling, which is more obvious in the enlarged EIS image after cycling (Figure 9c).

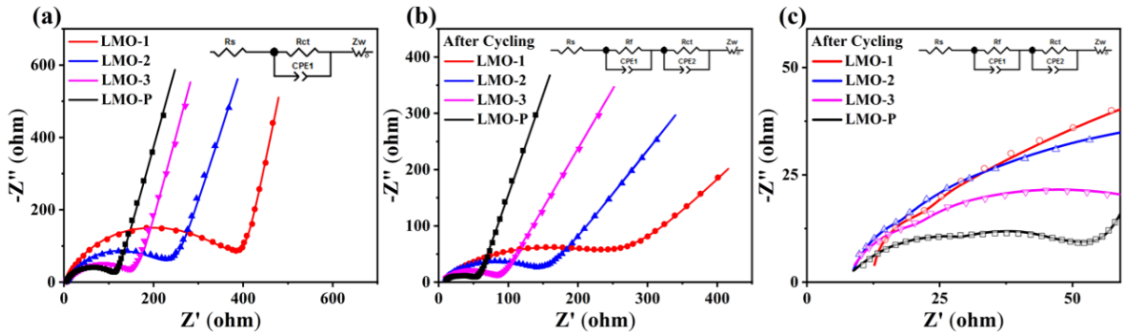

Figure 9. Electrochemical impedance spectra (EIS) of the various samples before (**a**) and after 15 cycles (**b**,**c**).

Table 3. Electrochemical parameters for the alternating current EIS results, calculated using Z-view software.

Samples	As Prepared		After Cycling		
	R_s (Ω)	R_{ct} (Ω)	R_s (Ω)	R_f (Ω)	R_{ct} (Ω)
LMO-1	5.56	384.19	12.71	23.53	237.61
LMO-2	5.88	274.01	8.80	24.88	134.10
LMO-3	5.52	146.73	8.99	27.53	64.07
LMO-P	5.38	112.42	8.75	29.41	30.44

Compared with the electrochemical properties of the $xLi_2MnO_3 \cdot (1-x)LiMnO_2$ cathode materials generated using various methods (Table 4), the superiority of those prepared using the dynamic hydrothermal route designed here is remarkable. Our synthetic procedure saves time, and the formation of the $0.072Li_2MnO_3 \cdot 0.928LiMnO_2$ nanocomposite leads to an optimum performance. The specific discharging capacity and cycling stability of the product are much better than the previously reported results, except for $0.23Li_2MnO_3 \cdot 0.77LiMnO_2$ produced via the solid-state method. However, in this composite, Li_2MnO_3 is activated after 20 cycles and does not show stability under extended cycling [11]. Modification strategies, including element doping and carbon composition, can also be implemented on the $xLi_2MnO_3 \cdot (1-x)LiMnO_2$ material to further improve the cycling stability and capacity, which will form the scope of future work.

Table 4. Summary of the synthetic conditions and electrochemical properties of the obtained lithium manganese oxide cathode materials prepared using different methods.

Product	Method	Voltage Range	Synthesis Condition	Current Density (mA g^{-1})	Maximum/Selected Cycle Discharge Capacity (mAh g^{-1})	Reference
$0.23Li_2MnO_3 \cdot 0.77LiMnO_2$	Solid state	2.0–4.5 V	750 °C/20 h	20	218/218 (30th)	[11]
$0.61Li_2MnO_3 \cdot 0.39LiMnO_2$	Sol–gel	2.0–4.8 V	600 °C/3 h 900 °C/12 h	10	177/167 (30th)	[12]
$0.44Li_2MnO_3 \cdot 0.56LiMnO_2$	Hydrothermal + solid state + pyrolysis reduction	2.0–4.8 V	200 °C/2 h 450 °C/10 h 500 °C/15 h 340 °C/4 h	30	270/200 (30th)	[13]
$H_{0.46}Li_{1.54}MnO_3$	Hydrothermal	2.0–4.8 V	180 °C/48 h	200	208/120 (20th)	[14]
$LiMnO_2-Li_2MnO_3$	Hydrothermal	2.0–4.5 V	200 °C/72 h	10	192/182 (5th)	[51]
o-$LiMnO_2$	Hydrothermal	2.0–4.5 V	160 °C/12 h	20	173/162 (20th)	[52]
Mixed m/o-$LiMnO_2$	Hydrothermal	2.0–4.5 V	m-$LiMnO_2$: 180 °C/4 h o-$LiMnO_2$: 180 °C/8 h o-$LiMnO_2$: 220 °C/8 h	20	m-$LiMnO_2$: 219.8/94.5 (50th) o-$LiMnO_2$: 198.8/112.5 (50th) o-$LiMnO_2$: 180.0/106.8 (50th)	[31]
o-$LiMnO_2$ nanorods	Solid state	2.0–4.25 V	750 °C/10 h	20	178.6/165.3 (40th)	[53]
Mesoporous o-$LiMnO_2$	Solid state	2.0–4.4 V	600 °C/3 h	20	191.5/162.6 (50th)	[54]
o-$LiMnO_2$	Dynamic hydrothermal	2.0–4.5 V	200 °C/3 h	30	166/145 (50th)	[28]
$0.072Li_2MnO_3 \cdot 0.928LiMnO_2$	Dynamic hydrothermal	2.0–4.8 V	200 °C/5 h	30	198.4/190.5 (50th)	This work

4. Conclusions

A series of $xLi_2MnO_3 \cdot (1 - x)LiMnO_2$ nanocomposites were prepared via a one-step dynamic hydrothermal method. A high concentration of alkaline solution, intense hydrothermal conditions, and stirring were used to produce nanoparticles that possess a large surface area and uniform dispersity. The composite characterized by a good crystallinity was found to be composed of orthorhombic $LiMnO_2$ and monoclinic Li_2MnO_3. The proportion of the two phases in the composite can be effectively controlled by the amount of oxygen in the autoclave, which, in turn, influences the electrochemical performance.

In contrast with most previously reported lithium-rich materials, the Li_2MnO_3 in this composite is completely inert, even when cycled at 2.0–4.8 V, and the typical activation reactions that contribute to extra capacity were not observed. This is ascribed to the high crystallinity and few faults in Li_2MnO_3; as an inert phase, Li_2MnO_3 effectively suppresses the structural distortion and collapse of the composite during cycling, which results in an improved cycling stability.

The composite with a $0.072Li_2MnO_3 \cdot 0.928LiMnO_2$ composition exhibited the best electrochemical performance and delivered a high capacity of 196.4 mAh g^{-1} at 0.1 C under 2–4.8 V. The capacity was maintained at 190.5 mAh g^{-1} with a retention rate of 97.0% by the 50^{th} cycle, which demonstrates an excellent cycling stability. This research describes a novel route to synthesize $xLi_2MnO_3 \cdot (1 - x)LiMnO_2$ cathode materials with a low cost and a stable cycling capability, for use in lithium-ion batteries.

Author Contributions: Conceptualization, L.-B.W. and C.-Q.S.; funding acquisition, L.-B.W. and C.-Q.S.; investigation, H.-S.H., Q.-H.X. and W.L.; methodology, H.-S.H., J.-D.G. and W.-K.C.; writing—original draft preparation, H.-S.H. and C.-Q.S.; writing—review and editing, C.-Q.S.; project administration, L.-B.W. All authors have read and agreed to the published version of the manuscript.

Funding: This research was funded by the National Natural Science Foundation of China (grant number 22075251), the Key Research and Development Program of Science and Technology Department of Zhejiang Province (grant number 2021C01176), and the Preferential Foundation of Zhejiang Province Postdoctoral Research Project (grant number ZJ2019075).

Institutional Review Board Statement: Not applicable.

Informed Consent Statement: Not applicable.

Data Availability Statement: The data that support the findings of this study are available from the corresponding author upon reasonable request.

Conflicts of Interest: The authors declare no conflict of interest. The funders had no role in the design of the study; in the collection, analyses, or interpretation of data; in the writing of the manuscript; or in the decision to publish the results.

References

1. Ozawa, K. Lithium-Ion Rechargeable Batteries with $LiCoO_2$ and Carbon Electrodes—The $LiCoO_2$/C System. *Solid State Ion.* **1994**, *69*, 212–221. [CrossRef]
2. Goodenough, J.B.; Park, K.S. The Li-ion rechargeable battery: A perspective. *J. Am. Chem. Soc.* **2013**, *135*, 1167–1176. [CrossRef]
3. Armand, M.; Tarascon, J.M. Building better batteries. *Nature* **2008**, *451*, 652–657. [CrossRef]
4. Whittingham, M.S. History, Evolution, and Future Status of Energy Storage. *Proc. IEEE* **2012**, *100*, 1518–1534. [CrossRef]
5. Zuo, W.H.; Luo, M.Z.; Liu, X.S.; Wu, J.; Liu, H.D.; Li, J.; Winter, M.; Fu, R.Q.; Yang, W.L.; Yang, Y. Li-rich cathodes for rechargeable Li-based batteries: Reaction mechanisms and advanced characterization techniques. *Energy Environ. Sci.* **2020**, *13*, 4450–4497. [CrossRef]
6. Su, X.; Wu, Q.L.; Li, J.C.; Xiao, X.C.; Lott, A.; Lu, W.Q.; Sheldon, B.W.; Wu, J. Silicon-Based Nanomaterials for Lithium-Ion Batteries: A Review. *Adv. Energy Mater.* **2014**, *4*, 1–23. [CrossRef]
7. Li, W.; Song, B.; Manthiram, A. High-voltage positive electrode materials for lithium-ion batteries. *Chem. Soc. Rev.* **2017**, *46*, 3006–3059. [CrossRef] [PubMed]
8. Chen, J.; Zou, G.Q.; Deng, W.T.; Huang, Z.D.; Gao, X.; Liu, C.; Yin, S.Y.; Liu, H.Q.; Deng, X.L.; Tian, Y.; et al. Pseudo-Bonding and Electric-Field Harmony for Li-Rich Mn-Based Oxide Cathode. *Adv. Funct. Mater.* **2020**, *30*, 2004302. [CrossRef]
9. Sun, Y.K.; Chen, Z.; Noh, H.J.; Lee, D.J.; Jung, H.G.; Ren, Y.; Wang, S.; Yoon, C.S.; Myung, S.T.; Amine, K. Nanostructured high-energy cathode materials for advanced lithium batteries. *Nat. Mater.* **2012**, *11*, 942–947. [CrossRef] [PubMed]

10. He, P.; Yu, H.; Li, D.; Zhou, H. Layered lithium transition metal oxide cathodes towards high energy lithium-ion batteries. *J. Mater. Chem.* **2012**, *22*, 3680–3695. [CrossRef]
11. Li, X.L.; Liu, D.J.; Zhang, D.W.; Chen, X.Y.; Tian, X.L. One-step synthesis and electrochemical behavior of $LiMnO_2$ and its composite from MnO_2 in the presence of glucose. *J. Phys. Chem. Solids* **2009**, *70*, 936–940. [CrossRef]
12. Saroha, R.; Gupta, A.; Panwar, A.K. Electrochemical performances of Li-rich layered-layered Li_2MnO_3-$LiMnO_2$ solid solutions as cathode material for lithium-ion batteries. *J. Alloys Compd.* **2017**, *696*, 580–589. [CrossRef]
13. Yang, F.; Zhang, Q.; Hu, X.; Peng, T. Synthesis of layered $xLi_2MnO_3\cdot(1-x)LiMnO_2$ nanoplates and its electrochemical performance as Li-rich cathode materials for Li-ion battery. *Electrochim. Acta* **2015**, *165*, 182–190. [CrossRef]
14. Huang, X.; Zhang, Q.; Chang, H.; Gan, J.; Yue, H.; Yang, Y. Hydrothermal Synthesis of Nanosized $LiMnO_2$–Li_2MnO_3 Compounds and Their Electrochemical Performances. *J. Electrochem. Soc.* **2009**, *156*, A162–A168. [CrossRef]
15. Zheng, J.; Myeong, S.; Cho, W.; Yan, P.; Xiao, J.; Wang, C.; Cho, J.; Zhang, J.G. Li- and Mn-Rich Cathode Materials: Challenges to Commercialization. *Adv. Energy Mater.* **2016**, *7*, 1601284. [CrossRef]
16. Yu, X.; Lyu, Y.; Gu, L.; Wu, H.; Bak, S.-M.; Zhou, Y.; Amine, K.; Ehrlich, S.N.; Li, H.; Nam, K.-W.; et al. Understanding the Rate Capability of High-Energy-Density Li-Rich Layered $Li_{1.2}Ni_{0.15}Co_{0.1}Mn_{0.55}O_2$ Cathode Materials. *Adv. Energy Mater.* **2014**, *4*, 1300950. [CrossRef]
17. Hy, S.; Felix, F.; Rick, J.; Su, W.N.; Hwang, B.J. Direct in situ observation of Li_2O evolution on Li-rich high-capacity cathode material, $Li[Ni_xLi_{1-2x/3}Mn_{2-x/3}]O_2$ ($0\leq x\leq 0.5$). *J. Am. Chem. Soc.* **2014**, *136*, 999–1007. [CrossRef]
18. Koga, H.; Croguennec, L.; Mannessiez, P.; Menetrier, M.; Weill, F.; Bourgeois, L.; Duttine, M.; Suard, E.; Delmas, C. $Li_{1.20}Mn_{0.54}Co_{0.13}Ni_{0.13}O_2$ with Different Particle Sizes as Attractive Positive Electrode Materials for Lithium-Ion Batteries: Insights into Their Structure. *J. Phys. Chem. C* **2012**, *116*, 13497–13506. [CrossRef]
19. Jarvis, K.A.; Deng, Z.Q.; Allard, L.F.; Manthiram, A.; Ferreira, P.J. Atomic Structure of a Lithium-Rich Layered Oxide Material for Lithium-Ion Batteries: Evidence of a Solid Solution. *Chem. Mater.* **2011**, *23*, 3614–3621. [CrossRef]
20. Rousse, G.; Tarascon, J.M. Sulfate-Based Polyanionic Compounds for Li-Ion Batteries: Synthesis, Crystal Chemistry, and Electrochemistry Aspects. *Chem. Mater.* **2013**, *26*, 394–406. [CrossRef]
21. Yang, J.S.; Li, P.; Zhong, F.P.; Feng, X.M.; Chen, W.H.; Ai, X.P.; Yang, H.X.; Xia, D.G.; Cao, Y.L. Suppressing Voltage Fading of Li-Rich Oxide Cathode via Building a Well-Protected and Partially-Protonated Surface by Polyacrylic Acid Binder for Cycle-Stable Li-Ion Batteries. *Adv. Energy Mater.* **2020**, *10*, 1904264. [CrossRef]
22. Gu, M.; Belharouak, I.; Zheng, J.; Wu, H.; Xiao, J.; Genc, A.; Amine, K.; Thevuthasan, S.; Baer, D.R.; Zhang, J.G.; et al. Formation of the spinel phase in the layered composite cathode used in Li-ion batteries. *ACS Nano* **2013**, *7*, 760–767. [CrossRef]
23. Lee, W.; Muhammad, S.; Sergey, C.; Lee, H.; Yoon, J.; Kang, Y.M.; Yoon, W.S. Advances in the Cathode Materials for Lithium Rechargeable Batteries. *Angew Chem. Int. Ed. Engl.* **2020**, *59*, 2578–2605. [CrossRef]
24. Nayak, P.K.; Erickson, E.M.; Schipper, F.; Penki, T.R.; Munichandraiah, N.; Adelhelm, P.; Sclar, H.; Amalraj, F.; Markovsky, B.; Aurbach, D. Review on Challenges and Recent Advances in the Electrochemical Performance of High Capacity Li- and Mn-Rich Cathode Materials for Li-Ion Batteries. *Adv. Energy Mater.* **2018**, *8*, 1702397. [CrossRef]
25. Assat, G.; Tarascon, J.M. Fundamental understanding and practical challenges of anionic redox activity in Li-ion batteries. *Nat. Energy* **2018**, *3*, 373–386. [CrossRef]
26. Hy, S.; Liu, H.D.; Zhang, M.H.; Qian, D.N.; Hwang, B.J.; Meng, Y.S. Performance and design considerations for lithium excess layered oxide positive electrode materials for lithium ion batteries. *Energy Environ. Sci.* **2016**, *9*, 1931–1954. [CrossRef]
27. Li, Q.; Li, G.S.; Fu, C.C.; Luo, D.; Fan, J.M.; Xie, D.J.; Li, L.P. Balancing stability and specific energy in Li-rich cathodes for lithium ion batteries: A case study of a novel Li-Mn-Ni-Co oxide. *J. Mater. Chem. A* **2015**, *3*, 10592–10602. [CrossRef]
28. Shen, C.Q.; Xu, H.; Liu, L.; Hu, H.S.; Chen, S.Y.; Su, L.W.; Wang, L.B. EDTA-2Na assisted dynamic hydrothermal synthesis of orthorhombic $LiMnO_2$ for lithium ion battery. *J. Alloys Compd.* **2020**, *830*, 154599. [CrossRef]
29. Fang, D.; Xie, J.L.; Hu, H.; Yang, H.; He, F.; Fu, Z.B. Identification of MnO_x species and Mn valence states in MnO_x/TiO_2 catalysts for low temperature SCR. *Chem. Eng. J.* **2015**, *271*, 23–30. [CrossRef]
30. Dong, J.Y.; Lu, G.; Yue, J.S.; Cheng, Z.M.; Kang, X.H. Valence modulation in hollow carbon nanosphere/manganese oxide composite for high performance supercapacitor. *Appl. Surf. Sci.* **2019**, *480*, 1116–1125. [CrossRef]
31. Li, X.H.; Su, Z.; Wang, Y.B. Electrochemical properties of monoclinic and orthorhombic $LiMnO_2$ synthesized by a one-step hydrothermal method. *J. Alloys Compd.* **2018**, *735*, 2182–2189. [CrossRef]
32. Zhang, X.D.; Shi, J.L.; Liang, J.Y.; Yin, Y.X.; Zhang, J.N.; Yu, X.Q.; Guo, Y.G. Suppressing Surface Lattice Oxygen Release of Li-Rich Cathode Materials via Heterostructured Spinel Li_4 Mn_5O_{12} Coating. *Adv. Mater.* **2018**, *30*, 1801751. [CrossRef] [PubMed]
33. Li, K.Y.; Shua, F.F.; Zhang, J.W.; Chen, K.F.; Xue, D.F.; Guo, X.W.; Komarneni, S. Role of Hydrothermal parameters on phase purity of orthorhombic $LiMnO_2$ for use as cathode in Li ion battery. *Ceram. Int.* **2015**, *41*, 6729–6733. [CrossRef]
34. Yang, F.; Zhang, Q.; Hu, X.; Peng, T.; Liu, J. Preparation of Li-rich layered-layered type x $Li_2MnO_3\cdot(1-x)LiMnO_2$ nanorods and its electrochemical performance as cathode material for Li-ion battery. *J. Power Source* **2017**, *353*, 323–332. [CrossRef]
35. Sun, Y.; Zan, L.; Zhang, Y.X. Enhanced electrochemical performances of Li_2MnO_3 cathode materials via adjusting oxygen vacancies content for lithium-ion batteries. *Appl. Surf. Sci.* **2019**, *483*, 270–277. [CrossRef]
36. Tang, S.B.; Lai, M.O.; Lu, L. Electrochemical studies of low-temperature processed nano-crystalline $LiMn_2O_4$ thin film cathode at 55 °C. *J. Power Source* **2007**, *164*, 372–378. [CrossRef]

37. Croguennec, L.; Deniard, P.; Brec, R.; Biensan, P.; Broussely, M. Electrochemical behavior of orthorhombic LiMnO2: Influence of the grain size and cationic disorder. *Solid State Ion.* **1996**, *89*, 127–137. [CrossRef]
38. Thackeray, M.M. Manganese oxides for lithium batteries. *Prog. Solid State Chem.* **1997**, *25*, 1–71. [CrossRef]
39. Pang, W.K.; Lee, J.Y.; Wei, Y.S.; Wu, S.H. Preparation and characterization of Cr-doped $LiMnO_2$ cathode materials by Pechini's method for lithium ion batteries. *Mater. Chem. Phys.* **2013**, *139*, 241–246. [CrossRef]
40. Jang, Y.I.; Huang, B.; Wang, H.; Sadoway, D.R.; Chiang, Y.M. Electrochemical Cycling-Induced Spinel Formation in High-Charge-Capacity Orthorhombic $LiMnO_2$. *J. Electrochem. Soc.* **2019**, *146*, 3217–3223. [CrossRef]
41. Kim, S.-W.; Pyun, S.-I. Lithium transport through a sol–gel derived LiMn2O4 film electrode: Analyses of potentiostatic current transient and linear sweep voltammogram by Monte Carlo simulation. *Electrochim. Acta* **2002**, *47*, 2843–2855. [CrossRef]
42. Francis Amalraj, S.; Markovsky, B.; Sharon, D.; Talianker, M.; Zinigrad, E.; Persky, R.; Haik, O.; Grinblat, J.; Lampert, J.; Schulz-Dobrick, M.; et al. Study of the electrochemical behavior of the "inactive" Li_2MnO_3. *Electrochim. Acta* **2012**, *78*, 32–39. [CrossRef]
43. Boulineau, A.; Croguennec, L.; Delmas, C.; Weill, F. Reinvestigation of Li_2MnO_3 Structure: Electron Diffraction and High Resolution TEM. *Chem. Mater.* **2009**, *21*, 4216–4222. [CrossRef]
44. Uyama, T.; Mukai, K.; Yamada, I. High-pressure synthesis and electrochemical properties of tetragonal $LiMnO_2$. *RSC Adv.* **2018**, *8*, 26325–26334. [CrossRef]
45. Shao-Horn, Y.; Hackney, S.A.; Armstrong, A.R.; Bruce, P.G.; Gitzendanner, R.; Johnson, C.S.; Thackeray, M.M. Structural Characterization of Layered $LiMnO_2$ Electrodes by Electron Diffraction and Lattice Imaging. *J. Electrochem. Soc.* **1999**, *146*, 2404–2412. [CrossRef]
46. Zhang, Q.; Peng, T.; Zhan, D.; Hu, X. Synthesis and electrochemical property of $xLi_2MnO_3 \cdot (1-x)LiMnO_2$ composite cathode materials derived from partially reduced Li_2MnO_3. *J. Power Source* **2014**, *250*, 40–49. [CrossRef]
47. Song, J.; Li, B.; Chen, Y.; Zuo, Y.; Ning, F.; Shang, H.; Feng, G.; Liu, N.; Shen, C.; Ai, X.; et al. A High-Performance Li-Mn-O Li-rich Cathode Material with Rhombohedral Symmetry via Intralayer Li/Mn Disordering. *Adv. Mater.* **2020**, *32*, 2000190. [CrossRef]
48. Zi, Z.Y.; Zhang, Y.T.; Meng, Y.Q.; Gao, G.; Hou, P.Y. Hierarchical Li-rich oxide microspheres assembled from {010} exposed primary grains for high-rate lithium-ion batteries. *New J. Chem.* **2020**, *44*, 8486–8493. [CrossRef]
49. Luo, X.D.; Yin, Y.Z.; Yuan, M.; Zeng, W.; Lin, G.; Huang, B.; Li, Y.W.; Xiao, S.H. High performance composites of spinel $LiMn_2O_4$/3DG for lithium ion batteries. *RSC Adv.* **2018**, *8*, 877–884. [CrossRef]
50. Vetter, J.; Novak, P.; Wagner, M.R.; Veit, C.; Moller, K.C.; Besenhard, J.O.; Winter, M.; Wohlfahrt-Mehrens, M.; Vogler, C.; Hammouche, A. Ageing mechanisms in lithium-ion batteries. *J. Power Source* **2005**, *147*, 269–281. [CrossRef]
51. Dang, F.; Hoshino, T.; Oaki, Y.; Hosono, E.; Zhou, H.; Imai, H. Synthesis of Li-Mn-O mesocrystals with controlled crystal phases through topotactic transformation of $MnCO_3$. *Nanoscale* **2013**, *5*, 2352–2357. [CrossRef] [PubMed]
52. Liu, Q.; Li, Y.X.; Hu, Z.L.; Mao, D.L.; Chang, C.K.; Huang, F.Q. One-step hydrothermal routine for pure-phased orthorhombic $LiMnO_2$ for Li ion battery application. *Electrochim. Acta* **2008**, *53*, 7298–7302. [CrossRef]
53. Zhao, H.Y.; Wang, J.; Wang, G.F.; Liu, S.S.; Tan, M.; Liu, X.Q.; Komarneni, S. Facile synthesis of orthorhombic $LiMnO_2$ nanorods by in-situ carbothermal reduction: Promising cathode material for Li ion batteries. *Ceram. Int.* **2017**, *43*, 10585–10589. [CrossRef]
54. Tong, W.M.; Chu, Q.X.; Meng, Y.J.; Wang, X.F.; Yang, B.; Gao, J.J.; Zhao, X.D.; Liu, X.Y. Synthesis of mesoporous orthorhombic $LiMnO_2$ cathode materials via a one-step flux method for high performance lithium-ion batteries. *Mater. Res. Express* **2018**, *5*, 065511. [CrossRef]